Mon. Not. R. Astron. Soc. **000**, 000–000 (0000) Printed 3 February 2022 (MN LATEX style file v2.2)

Reconstructing mass profiles of simulated galaxy clusters by combining Sunyaev–Zeldovich and X–ray images

S. Ameglio[1,2,3,4], S. Borgani[1,2,3], E. Pierpaoli[4], K. Dolag[5], S. Ettori[6,7] & A. Morandi[8]

[1] *Dipartimento di Astronomia dell'Università di Trieste, via Tiepolo 11, I-34131 Trieste, Italy (borgani@oats.inaf.it)*
[2] *INFN – National Institute for Nuclear Physics, Trieste, Italy*
[3] *INAF – Osservatorio Astronomico di Trieste, Trieste, Italy*
[4] *University of Southern California, Los Angeles, CA (ameglio,pierpaol@usc.edu)*
[5] *Max-Planck-Institut für Astrophysik, Karl-Schwarzschild Strasse 1, Garching bei München, Germany (kdolag@mpa-garching.mpg.de)*
[6] *INAF – Osservatorio Astronomico di Bologna, via Ranzani 1, I-40127 Bologna, Italy (ettori@oabo.inaf.it)*
[7] *INFN, Sezione di Bologna, viale Berti Pichat 6/2, I-40127 Bologna, Italy*
[8] *Dipartimento di Astronomia, Università di Bologna, via Ranzani 1, I-40127 Bologna, Italy (morandi@oabo.inaf.it)*

Accepted ???. Received ???; in original form ???

ABSTRACT

We present a method to recover mass profiles of galaxy clusters by combining data on thermal Sunyaev–Zeldovich (tSZ) and X–ray imaging, thereby avoiding to use any information on X–ray spectroscopy. This method, which represents a development of the geometrical deprojection technique presented in Ameglio et al. (2007), implements the solution of the hydrostatic equilibrium equation. In order to quantify the efficiency of our mass reconstructions, we apply our technique to a set of hydrodynamical simulations of galaxy clusters. We propose two versions of our method of mass reconstruction. Method 1 is completely model–independent and assumes as fitting parameters the values of gas density and total mass within different radial bins. Method 2 assumes instead the analytic mass profile proposed by Navarro et al. (1997) (NFW). We find that the main source of bias in recovering the mass profiles is due to deviations from hydrostatic equilibrium, which cause an underestimate of the mass of about 10 per cent at r_{500} and up to 20 per cent at the virial radius. Method 1 provides a reconstructed mass which is biased low by about 10 per cent, with a 20 per cent scatter, with respect to the true mass profiles. Method 2 proves to be more stable, reducing the scatter to 10 per cent, but with a larger bias of 20 per cent, mainly induced by the deviations from equilibrium in the outskirts. To better understand the results of Method 2, we check how well it allows to recover the relation between mass and concentration parameter. When analyzing the 3D mass profiles we find that including in the fit the inner 5 per cent of the virial radius biases high the halo concentration, thus suggesting that the NFW profile is not a perfect fit in the central regions of our simulations including cooling and star formation. Also, at a fixed mass, hotter clusters tend to have larger concentration. Our procedure recovers the concentration parameter essentially unbiased but with a scatter of about 50 per cent. In general, our analysis demonstrates that combining X–ray imaging with spatially resolved tSZ data is a valid alternative to using X–ray spectroscopy to recover the mass of galaxy clusters.

Key words: large-scale structure of Universe – galaxies: clusters: general – cosmology: miscellaneous – methods: numerical

1 INTRODUCTION

A number of important cosmological tests are based on mass measurements in galaxy clusters. In particular the mass function, the baryon fraction and their redshift evolution are highly sensitive to the underlying cosmology and provide constraints on the Dark Matter and Dark Energy content of the Universe. Precise mass measurement in galaxy cluster are then necessary to calibrate clusters as precision tools for cosmology (Haiman et al. 2001; Rosati et al. 2002; Pierpaoli et al. 2003; Voit 2005; Borgani 2006).

In X–ray studies, the total collapsed mass of a cluster is determined by applying the hydrostatic equilibrium equation to gas density and temperature profiles. A number of authors (e.g., Rasia et al. 2004; Kay et al. 2004; Nagai et al. 2007) analyzed hydrodynamical simulations of galaxy clusters and found that the gas is not in perfect hydrostatic equilibrium. Instead, they found deviations up to 20 per cent, which have the effect of systemat-

ically biasing low the reconstruction of the total collapsed mass. The amount of this underestimate depends on both the model assumed and the dynamical state of the cluster. For instance, Rasia et al. (2006) showed that assuming the isothermal β–model (Cavaliere & Fusco-Femiano 1976) for the gas distribution gives the worst reconstruction. Nagai et al. (2007) differentiated their sample of simulated clusters in relaxed and unrelaxed objects, with the latter showing a larger scatter in the mass reconstruction. Following the same direction, Jeltema et al. (2007) found a correlation between quantitative measures of the morphology of the X–ray images and the bias in the mass reconstruction, although with a quite large scatter. Puchwein & Bartelmann (2007) probed the deviations from hydrostatic equilibrium in different stages of a merger process, while Piffaretti & Valdarnini (2008) performed an extended analysis of a large sample (~ 100) of simulated galaxy clusters, in order to disentangle various biases in the mass reconstruction.

Recovering mass profiles via the hydrostatic equilibrium equation involves the derivatives of both gas density and temperature profiles. Then, an accurate mass determination requires high–quality temperature measurements. For this reason, X–ray studies are often limited to the inner regions of the clusters and to objects at moderate redshift. Furthermore, all the temperature profiles so far used for the reconstruction of cluster masses are based on X–ray data. As originally noticed by Mazzotta et al. (2004) (see also Vikhlinin 2006), the thermal complexity of the ICM causes the temperature determined by fitting the X–ray spectrum to a single–temperature bremsstrahlung model to be generally different from the electron temperature. On the other hand, it is the electron temperature that enters in the equation of hydrostatic equilibrium (under the assumptions of fully ionized plasma and equilibration between ions and electrons). The question then arises as to whether the difference between spectroscopic and electron temperature may induce an additional bias in the mass estimate.

In this paper, we propose to use a combination of X–ray imaging and tSZ data, which avoids the use of X–ray spectroscopy. Taking advantage of the different dependence of the tSZ signal and of the X–ray emissivity on gas density and temperature, one can recover both by suitably deprojecting tSZ and X–ray imaging data, without the need of any X–ray spectroscopic information. Furthermore, both X–ray and SZ cluster images can be obtained in principle out to larger radii than possible for X–ray spectra. Therefore, their combination could allow studies of the ICM thermal properties to be pushed out to larger fractions of the whole cluster virialized regions. Indeed, different algorithms, which use a combination of tSZ and X–ray data, have been proposed by a number of authors and applied to analytical cluster models and/or sets of simulated clusters (e.g. Zaroubi et al. 2001; Lee & Suto 2004; De Filippis et al. 2005; Puchwein & Bartelmann 2007; Ameglio et al. 2007, and references therein). Owing to the relatively low angular resolution of currently available tSZ telescopes, this method has been so far applied only to a handful of observed clusters (Zhang & Wu 2000; Pointecouteau et al. 2002; Mroczkowski et al. 2008), with results that are generally consistent with those based on X–ray spectroscopic data.

Accurate mass profiles reconstruction can also be used as probes for cosmology. In fact, mass profiles are expected to follow a universal functional form, which is valid over a wide range of masses, from dwarf galaxies to massive galaxy clusters. A formulation for this function has been originally provided by fitting the mass profiles in a set of N–body simulations by Navarro et al. (1997) (NFW hereafter). The analysis of X–ray data from Chandra and XMM–Newton observations confirm the validity of the NFW model, out to a significant fraction of the cluster virial radius (e.g. Pratt & Arnaud 2002; Pointecouteau et al. 2005; Vikhlinin et al. 2006; Zappacosta et al. 2006). An important parameter of the NFW model is the concentration c, which is given by the ratio between the halo's virial radius and the characteristic radius of the density profile. In the hierarchical structure formation scenario the more massive objects are expected to form recently, from a lower–density environment than less massive ones. Thus, it is expected an inverse correlation between the mass of an object and its concentration, with a substantial scatter related to the distribution of halo formation epochs (e.g., Navarro et al. 1997; Bullock et al. 2001; Dolag et al. 2004). This relation has been confirmed by the observation of mass profiles in galaxy clusters, using both X-ray and lensing data (Schmidt & Allen 2007; Mandelbaum et al. 2008, and references therein). These authors generally agree in finding a well defined relation with a substantial intrinsic scatter, as expected from the predictions of numerical simulations. However, some discrepancies are still present in the determination of the slope and normalization of the relation, which may be generated by biases in the mass measurements and/or by selection effects.

We extend here the deprojection algorithm presented by Ameglio et al. (2007) (A07 hereafter), by including the solution of the hydrostatic equilibrium equation. Using this technique, we analyze a set of 14 simulated clusters having $T_{\rm sl}\gtrsim 3$ keV, with the aim of quantifying the accuracy with which total mass profiles can be recovered by combining X–ray and tSZ images. We will also discuss how the relation between halo concentration c and mass M can be recovered with our deprojection method, also comparing it with the theoretical predictions of the model by Eke et al. (2001). The analysis presented in the following can be applied to data from the present generation of X–ray telescopes. Furthermore, future X–ray observations with lower background (e.g. as expected from the eROSITA mission[1]) will provide good imaging data for a large number of clusters out to $z \simeq 1$. As for the tSZ data, exploiting the full potentiality of our technique would require spatially resolved observations, which will be available from upcoming (or just started) SZ experiments, based both on interferometric arrays (ALMA: Atacama Large Millimeter Array[2]; CARMA: Combined Array for Research in Millimeter-wave Astronomy[3]) and on single dishes with large bolometer arrays (CCAT: Cornell–Caltech Atacama Telescope [4]; LMT: Large Millimeter Telescope[5]).

The paper is structured as follows. In Section 2 we briefly present the set of simulated clusters. We use the same subset of simulated clusters having $T_{sl}\gtrsim 3$ keV, which is described by A07. In Section 3 we introduce the hydrostatic equilibrium equation and, as a preliminary test, probe the intrinsic deviations from this equilibrium for our set of simulated clusters. After briefly reviewing the deprojection algorithm introduced by A07, Section 4 describes the implementation of the hydrostatic equilibrium equation in this algorithm. Sections 5 and 6 present our results on the total mass reconstruction and on the c–M relation respectively. Finally, our main conclusions are summarized in Section 7.

[1] http://www.mpe.mpg.de/projects.html#erosita
[2] http://www.eso.org/projects/alma/
[3] http://www.mmarray.org
[4] http://astrosun2.astro.cornell.edu/research/projects/atacama/
[5] http://www.lmtgtm.org/

2 THE SET OF SIMULATED CLUSTERS

The sample of simulated galaxy clusters used in this paper has been extracted from a large-scale cosmological hydro-N-body simulation of a "concordance" ΛCDM model with $\Omega_m = 0.3$ for the matter density parameter, $\Omega_\Lambda = 0.7$ for the cosmological constant, $\Omega_{\rm b} = 0.019\,h^{-2}$ for the baryon density parameter, $h = 0.7$ for the Hubble constant in units of 100 km s^{-1}Mpc^{-1} and $\sigma_8 = 0.8$ for the r.m.s. density perturbation within a top–hat sphere having comoving radius of $8\,h^{-1}{\rm Mpc}$ (see Borgani et al. 2004, for further details). The simulation, performed with the Tree+SPH code GADGET-2 (Springel 2005), follows the evolution of 480^3 dark matter particles and an initially equal number of gas particles in a periodic cube of size $192h^{-1}$ Mpc. The mass of the gas particles is $m_{\rm gas} = 6.9 \times 10^8 h^{-1} M_\odot$, and the Plummer-equivalent force softening is $7.5h^{-1}$ kpc at $z = 0$. The simulation includes the treatment of radiative cooling, a uniform time–dependent UV background, a sub–resolution model for star formation and energy feedback from galactic winds (Springel & Hernquist 2003). At $z = 0$ we extract a set of 117 clusters, whose mass, as computed from a friends-of-friends algorithm with linking length $b = 0.15$ (in units of the mean interparticle distance) is larger than $10^{14}\,h^{-1}M_\odot$. For these clusters we compute the spectroscopic–like temperature

$$T_{sl} = \frac{\sum_i n_{e,i}^2 T_i^{a-1/2}}{\sum_i n_{e,i}^2 T_i^{a-3/2}}\,, \qquad (1)$$

where $a = 0.75$ is a parameter shown by Mazzotta et al. (2004) to accurately reproduce the temperatures obtained from the spectroscopic fit.

Due to the limited box size, the largest cluster found in the cosmological simulation has $T_{\rm sl} = 4.6$ keV. In order to extend our analysis to more massive and hotter systems, which are mostly relevant for current tSZ observations, we include four more galaxy clusters having $M_{\rm vir} > 10^{15}\,h^{-1}M_\odot$[6] and belonging to a different set of hydro-N-body simulations (Borgani et al. 2006). These objects have been selected from a DM–only simulation of a large cosmological volume (Yoshida et al. 2001), and resimulated at higher resolution. The achieved resolution corresponds to $m_{\rm gas} = 1.69 \times 10^8 h^{-1} M_\odot$ for the mass of the gas particle and a gravitational softening of $5h^{-1}$kpc at $z = 0$. These simulations have been performed with the same choice of the parameters defining star–formation and feedback. The cosmological parameters also are the same, except for a higher power spectrum normalization, $\sigma_8 = 0.9$.

From this large set of simulated clusters, we select a subsample of objects having $T_{sl} \gtrsim 3$ keV, which are more relevant for SZ studies. We identify 15 suitable objects, from which we exclude one very irregular cluster. The main characteristics of this subset of simulated clusters are listed in Table 1, where the cluster labeled C4, C12, C13 and C14 are those based on the high–resolution resimulations. All the results shown in this paper are based on the analysis of these 14 objects. A larger subsample of systems with $T_{sl} < 3$ keV, extracted from the same box, are used for the analysis presented in Section 6.

[6] Here and in the following, the virial radius, $r_{\rm vir}$, is defined as the radius of a sphere centred on the local minimum of the potential, containing an average density, $\rho_{\rm vir}$, equal to that predicted by the spherical collapse model. For the cosmology assumed in our simulations at low redshift it is $\rho_{\rm vir} \simeq 100\rho_{\rm c}$, being $\rho_{\rm c}$ the cosmic critical density. Accordingly, the virial mass, $M_{\rm vir}$, is defined as the total mass contained within this sphere.

Cluster	M_{vir} $10^{14}M_\odot$	T_{sl} keV	r_{vir} Mpc	r_{500} Mpc
C1	5.4	3.1	2.1	1.0
C2	10.1	4.3	2.6	1.3
C3	18.6	4.6	3.2	1.5
C4	21.4	6.8	3.3	1.7
C5	9.9	4.5	2.6	1.3
C6	5.7	3.1	2.1	1.0
C7	7.1	3.6	2.3	1.1
C8	5.8	3.2	2.2	1.1
C9	4.8	3.0	2.0	1.0
C10	4.8	3.0	2.0	1.0
C11	6.3	3.0	2.2	1.0
C12	32.0	8.9	3.8	1.9
C13	19.2	6.3	3.2	1.6
C14	19.4	5.7	3.2	1.6

Table 1. Characteristics of the simulated clusters, having $T_{\rm sl} \gtrsim 3$ keV, to which we apply the deprojection procedure. Col. 2: virial mass; Col. 3: spectroscopic–like temperature; Col. 4: virial radius; Col. 5: r_{500}.

We generate synthetic X–ray and tSZ maps of these clusters, to which we apply our method of mass reconstruction. Our procedure of map making is described in detail in A07, while here we summarize the most important characteristics: *i*) we generate three maps of each cluster, by projecting it on the principal axes of the inertia tensor, so that the projection on the x, y and z axes represent the projection along the minimum, medium and maximum elongation of the cluster, respectively; *ii*) the X–ray maps are obtained by Montecarlo generation of 10^4 photon counts from the surface brightness maps in the [0.5-2] keV energy band, after smoothing it with a PSF having a FWHM of 0.5 arcsec (comparable to the Chandra one at the aim point), without adding the contribution from any instrumental or cosmic background; *iii*) the noise setup for the tSZ maps is modeled on the Cornell Caltech Atacama Telescope (CCAT). The maps are convolved with a Gaussian beam having FWHM$= 0.44'$ and then it is added a white noise. In order to have approximately the same signal–to–noise for all objects, the noise level is 3 μK/beam for clusters with $T_{\rm sl} < 4$ keV and 10 μK/beam for the hotter ones.

In the following, we will show detailed results on the recovery of total mass profiles for a subset of 4 clusters, which are indicated in Table 1 with C1–4. The first three of them are extracted from the cosmological hydrodynamical simulation, while C4 is one of the massive clusters simulated at higher resolution. C2, C3 and C4 are typical examples of clusters at low, intermediate and high temperature, while C1 is an interesting case to understand the effect of fore–background contaminations. These four clusters have been used also in A07 as examples.

3 THE HYDROSTATIC EQUILIBRIUM

Total mass profiles from observations of the ICM are computed by assuming that the gas lies in hydrostatic equilibrium (HE hereafter) within the cluster gravitational potential. In the case of spherical symmetry, the equation of hydrostatic equilibrium can be cast in the form

$$M_{tot}(<r) = -\frac{kT(r)\,r}{G\mu m_p}\left[\frac{d\ln n_e}{d\ln r} + \frac{d\ln T}{d\ln r}\right]\,, \qquad (2)$$

where $T(r)$ is the temperature at the radius r, μ the mean molecular weight ($\mu \simeq 0.6$ for a gas of primordial composition), and m_p the proton mass. Note that the mass at a given radius depends only

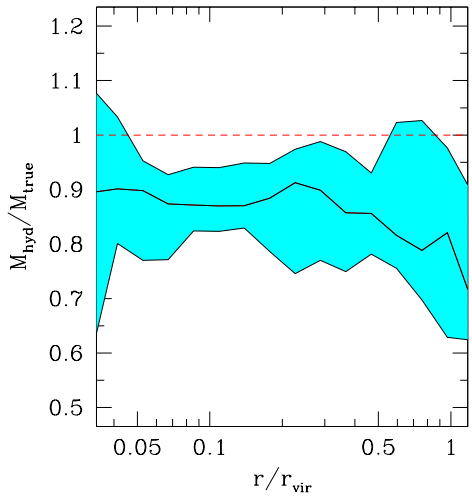

Figure 1. The ratio between the hydrostatic and the true mass profiles, averaged over the set of simulated clusters. The shaded area encompasses the 16 and 84 percentiles, while the central continuous line shows the average profile of the deviation.

upon the local pressure derivative and is unaffected by the physical properties of the cluster at smaller or larger radii.

While to first approximation clusters are quite close to the condition of pressure equilibrium, small but sizable deviations are generally found in the analysis of simulated clusters (e.g., Rasia et al. 2004; Kay et al. 2004; Dolag et al. 2004; Rasia et al. 2006; Nagai et al. 2007; Piffaretti & Valdarnini 2008). These deviations are generally ascribed to the presence of non–negligible stochastic gas motions, which provide an effective non–thermal pressure support, thereby leading to an underestimate of the total gravitating mass when not accounted for in eq. (2). Rasia et al. (2004) suggested the addition of an extra–term, which takes into account the presence of gas motions, to the equation of the hydrostatic equilibrium. Jeltema et al. (2007) find a correlation between the amount of substructures and the underestimate of the total mass, in a set of hydrodynamical simulations. However, the large scatter in this correlation around the mean relation suggests that substructures may not be the only sources of the bias in the mass reconstruction.

Before applying our procedure of mass reconstruction, we assess the degree of violation of HE in our clusters. This will allow us to quantify by how much the differences between reconstructed and true mass profiles are due to biases in the deprojection method or to violation of the HE.

We apply eq. (2) to the true, 3-D density and temperature profiles, by performing a numerical derivative in the log-log space, using a 3–point Lagrangian interpolation[7]. We will refer to the mass so computed as the hydrostatic mass, M_{hyd} hereafter. In Figure 1 we show the profiles of the ratio M_{hyd}/M_{true} averaged over our set of simulated clusters, along with the 1σ scatter around the mean. We generally find that the hydrostatic masses underestimate the true ones on average by ~ 10 per cent out to about r_{500}, a result which is in line with those found by other analyses of simulated clusters (e.g., Nagai et al. 2007; Puchwein & Bartelmann 2007; Jeltema et al. 2007). At larger radii this underestimate increases, reaching about 20 per cent at r_{vir}, along with an increase of the scatter. This is consistent with the expectation that outer cluster regions deviate more from the condition of HE, due to the presence of ongoing mergers and continuous gas accretion.

[7] The profile of $\log(nT)$ is computed for log-equispaced values of r. To compute the derivative at a given radius, we fit with the point of interest and its two adjacent ones with a quadratic curve. The first-order derivative at the middle point is taken to be the derivative of the profile at that radius.

4 METHODS OF MASS PROFILE RECONSTRUCTION

The methods described here, aimed at recovering the cluster mass profiles, represent a development of the MonteCarlo Markov Chain (MCMC) maximum likelihood deprojection technique described in A07. The algorithm is modified in order to solve the hydrostatic equilibrium equation while deprojecting the cluster images. In this way, the temperature profile is computed from the gas density and total mass profiles, so that all quantities are derived simultaneously and in a fully self–consistent way. We provide here below only a brief description of the deprojection technique, while we refer to A07 for further details.

The cluster is assumed to have a onion-skin structure, with N concentric spherical shells, having uniform gas properties (gas density and temperature). The image of the cluster (in both tSZ and X–ray) is divided into N rings, which have the same limiting radii of the shells for sake of simplicity. The tSZ and X–ray profiles are then computed by projecting this onion-skin model in the plane of the sky. We divide the virial radius and r_{500} into $N = 14$ and $N = 10$ rings, respectively, equally spaced in logarithm. This solution represents a good compromise between the resolution of the profiles and the noise level. Finally, the inner 50 kpc of all clusters are excluded by all fits.

The deprojection is then performed by the maximization of a likelihood function, which is computed by comparing the observed tSZ and X–ray surface brightness profiles with the ones obtained from the model. This approach has the advantage of deprojecting of both X–ray and tSZ profiles simultaneously, directly obtaining the whole gas density and temperature and total mass profiles, along with the corresponding uncertainties. Moreover, it is possible to introduce in the likelihood extra terms in order to improve the accuracy and robustness of the technique. In particular, we adopt a regularization constraint, based on the Philips-Towmey regularization method (Bouchet 1995, and references therein). This method has been already used also by Croston et al. (2006) to deproject X–ray imaging and spectral data. It works by interpolating with a quadratic curve each group of three consecutive points in the profile and then minimizing the second derivative (i.e. the curvature) of such curves at the position of the middle point (see A07 for a more detailed description). The general effect of the regularization is to smooth out oscillations in the profiles, which are due either to genuine substructures or to noise which propagates from adjacent bins in the deprojection.

We define a joint likelihood for the tSZ profile, $\mathcal{L}_{tSZ}$, and for the X–ray surface brightness profile, $\mathcal{L}_{Xray}$, also including a term associated to the regularization constraint, $\mathcal{L}^{\lambda}_{reg}$. Since these three terms are independent, the total likelihood is given by the product of the individual ones:

$$\mathcal{L} \equiv \mathcal{L}_{tSZ} \cdot \mathcal{L}_{Xray} \cdot \mathcal{L}^{\lambda}_{reg}. \quad (3)$$

The fitting parameters are represented by the gas density and total mass profiles (plus the external pressure). The algorithm first computes the temperature profile from the density and mass pro-

files by inverting the hydrostatic equilibrium equation; then the gas density and temperature profiles are combined to compute the projected model profiles of X–ray and tSZ; finally these model profiles are compared to those obtained from the mock observations to compute the joint likelihood. As for the gas density profile, our approach is completely model–independent, since we treat its value into each spherical shell as a free parameter, as described in A07. As for the reconstruction of the total mass profiles, we adopt two different approaches. Both methods are described in Ettori et al. (2002) for the application to X–ray datasets, although with a different implementation. Also, Morandi & Ettori (2007) present a refined version of these methods for the study of high resolution X-ray observations, while Rasia et al. (2006) discuss their limitations by applying them to a set of hydrodynamical simulations.

- **Method 1**. This method consists in the direct numerical inversion of the HE equation. It does not assume any particular functional form for the mass profile. Instead, the integrated mass enclosed by the mean radius of each shell is treated as a free parameter. The only constraint that we impose is that the mass has to increase with radius, in order to avoid unphysical solutions. The advantage of this method is that it provides a completely model–independent reconstruction of the mass profile, which relies only on the assumption of hydrostatic equilibrium.
- **Method 2**. This method is based on assuming the functional form for the mass profile provided by the NFW model. Its major advantage with respect to Method 1 is that the reconstruction becomes more stable, at the cost of assuming a particular model for the mass profile. The NFW model is widely adopted in the mass reconstruction from X–ray observations. These analyses showed that it provides a remarkably good description of the mass profiles of massive galaxy clusters, out to large portions of their virial radii (see also, e.g. Pointecouteau et al. 2005; Vikhlinin et al. 2006; Gastaldello et al. 2007). The NFW expression for the mass profile reads

$$M(<r) = 4\pi r_s^3 \rho_{crit} \delta_c f(x) \tag{4}$$

where r_s is a characteristic scale length, $x = r/r_s$ is the distance from the halo centre in units of r_s, $f(x) = ln(1+x) - x/(1+x)$, ρ_{crit} is the critical cosmic density and δ_c is a characteristic overdensity. It is common (and more convenient) to rewrite the above equation by expressing δ_c as a function of the concentration parameter $c = r_\Delta/r_s$, where Δ is a given overdensity. Here and in the following, we adopt for Δ the value of the density contrast at virialization predicted by the spherical collapse model, which corresponds to $\Delta \simeq 100$ in our cosmology (e.g., Eke et al. 1996). The characteristic overdensity is then written as

$$\delta_c = \frac{\Delta}{3} \frac{c^3}{f(x=c)}\,, \tag{5}$$

so that the NFW profile becomes

$$M(<r) = \frac{4\pi}{3}(r_s c)^3 \rho_{crit} \Delta \frac{f(x)}{f(x=c)} \equiv M_\Delta \frac{f(x)}{f(x=c)}\,. \tag{6}$$

As for the temperature profile, it is then computed in both methods from the model mass profile, under the HE assumption (see Section 3). By inverting the HE equation one first obtains the gas pressure profile and then the gas temperature, by combining pressure with gas density. In this way we obtain

$$kT(r) = -\frac{1}{n_e(r)} \left\{ G\mu m_p \int_{r_{out}}^{r} \frac{n_e M(<r)}{r^2} dr - P(r_{out}) \right\}\,. \tag{7}$$

In the above equation the integral is performed from the outermost radius from which the deprojection is performed, r_{out}, and the radius of interest r, while P_{out} is the electron pressure at $r = r_{out}$. In both methods, we apply the regularization constraint to the temperature profile, in order to smooth out spurious fluctuations which are essentially due to the presence of noise. The regularization term in the likelihood is given by (see A07 for further details):

$$ln(\mathcal{L}^\lambda_{reg}) \equiv -\lambda \sum_{i=3}^{N-1} (2f_i - f_{i-1} - f_{i+1})^2 \tag{8}$$

where $\lambda = 2.5$ and f_i is the value of the temperature in keV in the i-th bin.

Since the hydrostatic equilibrium equation constraints only the pressure difference between two points, it is necessary to introduce a further parameter $P(r_{out})$ (see also Morandi et al. 2007). In particular, in the case of Method 1 this parameter is completely degenerate with the mass enclosed in the outermost bin. The mass has only a lower boundary, given by the fact that it cannot be lower than the mass enclosed by the inner bin. This turns into an instability of the fit which generates an overestimate of the global mass. This problem is solved by applying the regularization constraint to the pressure profile. In this way, in Method 1 the regularization constraint is actually applied in two places. Note that once the temperature profile is regularized, the pressure profile becomes regular as well, so its contribution to the global likelihood turns out to be generally small. The regularization of the pressure profile is more important in the outermost two bins, where it is used to break the degeneracy between P_{out} and the total mass. So, in Method 2 we insert in the likelihood a second regularization term, which has the same structure of eq. (8), where now $\lambda = 5$ and f_i is the logarithm of the pressure in the i-th bin. Note that the numerical value of λ does not give a direct indication of the weight given to regularization, because this depends on the units used for the quantity f_i.

Given the high number of fitting parameters ($2N + 1$ for Method 1, $N + 3$ for Method 2 respectively), we apply a MCMC technique, which is described in A07. The technique has the advantage of computing the (marginalized) probability distribution of all parameters simultaneously, together with the whole covariance matrix. For a more detailed information on MCMC fitting techniques we refer to Neal (1993), Gilks et al. (1996) and MacKay (1996).

5 RESULTS

As already pointed out, both methods of mass reconstruction adopt a different implementation with respect to the deprojection technique presented in A07. Reassuringly enough, the gas density and temperature profiles obtained from all methods are virtually identical. For this reason, they are not shown in the following while we will concentrate our discussion only on the mass reconstruction.

5.1 Total mass profiles: method 1

We show in Figure 2 the comparison between the reconstructed and the true mass profiles for the C1–4 clusters, chosen as examples. We generally find an underestimate by about 10–15 per cent throughout the virial radius, with slightly larger deviations in the centre and in the outskirts. For all these four clusters (and for most of the others) the uncertainties in X–ray and tSZ profiles do not allow us to place tight constraints on the amount of mass contained within the innermost bin. Since this quantity has no lower boundary (e.g.

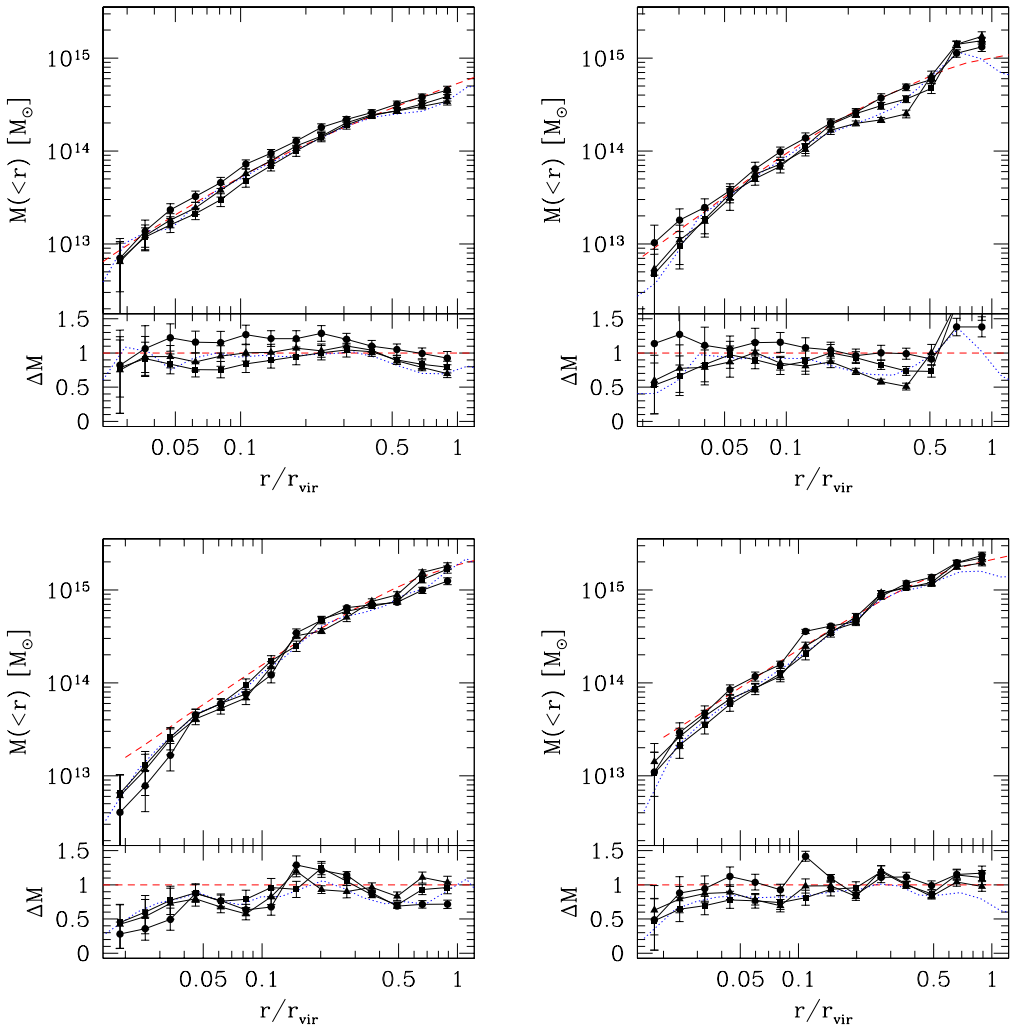

Figure 2. Mass reconstruction for the clusters C1 (upper left), C2 (upper right), C3 (lower left) and C4 (lower right), while applying Method 1. The black triangles (squares, circles) and line represent the reconstruction along the x (y, z) axis. The red dashed line represents the true mass profile, while the blue dotted line is hydrostatic mass obtained from the application of eq. (2) to the true 3–dimensional gas density and temperature profiles. The lower part of each panel shows the ratio between the same quantities and the true mass.

given by the mass contained within an inner bin), we find cases in which the lower limit of this mass takes very low or even negative values. To avoid this problem, we fix by hand a lower limit for the mass within the innermost bin at $10^{12}\,h^{-1}M_{\odot}$. A comparison of the reconstructed mass profiles with the profiles of hydrostatic mass, M_{hyd}, generally show a close agreement. This demonstrates that the main source of systematics is intrinsic, namely the deviation of the gas from a perfect hydrostatic equilibrium, while the deprojection method is essentially unbiased. While this is strictly true out to $r \simeq 0.5r_{vir}$, we note a tendency for the reconstructed mass to lie above M_{hyd} when approaching the virial radius. We attribute this to the lower signal–to–noise ratio in the external regions (SNR $\sim 4-5$ for both the SZ and X–ray signals in the outermost bin, compared to 15–20 in the innermost bins) and to a larger impact of fore/background contaminations in these regions. In fact, the recovered mass at these radii is bound not to be smaller than the mass at the inner radii, while it does not have any upper boundary. As a consequence, any deviation associated to noise or contamination can only act in the direction of increasing the mass. We further point out that our synthetic X–ray maps do not include a background, so the noise here is only given by the poissonian noise of the signal. Clearly, the inclusion of a realistic background would limit our analysis to scales comparable to those reached by X–ray observations, which only in some cases trace the emissivity beyond $\sim r_{200}$ (Neumann 2005).

These results are also confirmed from the analysis of the whole set of simulated clusters. Indeed, Figure 3 shows that in the inner regions (out to about $r = 0.15r_{vir}$) the mass profile recovered from our deprojection algorithm are quite close on average to the hydrostatic masses, while being consistently smaller that the true mass profiles, by about 10–15 per cent. Instead, in the outskirts the reconstructed mass profiles seem to well recover the true ones. However, this agreement is due to the effect of two biases, namely a violation of HE and the effect of noise in the deprojection algorithm, which act in opposite direction, rather than to an intrinsically better performance of the deprojection method at large radii.

In A07 we showed that the C1 cluster has a significant contamination in the projection along the z axis, due to a merging group

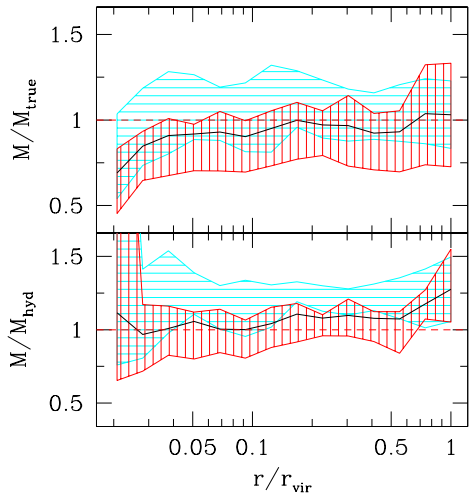

Figure 3. Reconstructed vs. true (upper panel) and hydrostatic (lower panel) mass, averaged over the set of simulated clusters, while applying Method 1. In each panel, the horizontally (vertically) shaded area represents the mean$\pm 1\sigma$ over the projections along the z (x and y) axis. The black line represents the mean over all the projections of all clusters.

which is approaching the cluster virial region. The effect of this contamination was to boost the temperature profile by about 20 per cent. In the upper left panel of Figure 2 we show that this causes a mass overestimate by a comparable amount of the mass reconstructed from the projection along the z axis, which lies above the hydrostatic mass in this particular case. Also for the C2, C3 and C4 clusters the mass reconstructed from the projection along the axis of maximum elongation is larger than the mass recovered from the other two projections. Figure 3 confirms that this behaviour is still present when averaging over the whole set of simulated clusters.

5.2 Total mass profiles: method 2

We show in Figure 4 the mass profiles of the same 4 clusters chosen as examples, as reconstructed from the application of the method based on assuming an NFW model. In this case, the reconstructed profiles are not reported with errorbars, which are assigned to the total mass M and to the concentration parameter c, which are the only two parameters entering in the fitting procedure. The accuracy in recovering these parameters is discussed in the following.

Clearly, assuming an analytical form for the mass profiles has the advantage of providing a much more stable reconstruction and a smooth profile. Similarly to the case of the Method 1, the recovered mass is much closer to the hydrostatic mass than to the true one. The left panel of Figure 5 shows the accuracy of the recovered mass profile, after averaging over the whole set of simulated clusters. From the upper panel of this plot, we note that the mass profile is generally underestimated by about 15–20 per cent. The slightly larger underestimate with respect to Method 1 is due to the fact that here we are adopting an analytical model. We remind that the violation of hydrostatic equilibrium is larger at r_{vir}, which is the outermost radius from which the reconstruction of the mass profile begins. Since we force the profile to follow the NFW shape when reconstructing at smaller radii, this larger mass underestimate is now propagated inward. This is different from what happens for the Method 1, where the value of the mass at an inner radius is not forced by the extrapolation of the profile recovered at a larger radius. The right panel of Figure 5 shows the accuracy in recovering the total mass as a function of the true mass of the cluster. We find that the statistical uncertainties in the estimate of the cluster masses are generally smaller than the bias induced by the violation of the hydrostatic equilibrium and are also smaller than the scatter associated to the choice of the projection direction. This panel also shows the presence of an outlier, which is the cluster labeled C5; this object has a much more irregular structure when compared with the rest of the sample. For this reason, here and in the following we exclude it from the computation of the mean and the standard deviation over the sample of simulated clusters, as reported in Table 2. Within r_{vir}, we find $M_{rec}/M_{true} = 0.81 \pm 0.10$, with no significant dependence on the cluster mass.

	Δ	$\frac{M_\Delta(< r_{\Delta,sim})}{M_{\Delta,true}}$	$\frac{r_{\Delta,fit}}{r_{\Delta,true}}$	$\frac{M_\Delta(r_{\Delta,fit})}{M_{\Delta,true}}$
$r < r_{vir}$	vir	0.81 ± 0.10	0.91 ± 0.05	0.77 ± 0.11
$r < r_{500}$	500	0.89 ± 0.16	0.95 ± 0.08	0.87 ± 0.20
	vir	0.90 ± 0.21	0.95 ± 0.10	0.89 ± 0.27

Table 2. Summary of the results of Method 2 over the whole set of simulated clusters. The first column reports the limiting radius of the fit, while the second column reports the overdensity Δ at which all quantities are computed. Columns 3 to 5 report the mean and standard deviation for the accuracy in recovering the following quantities: the total mass within R_Δ when it is computed from simulation data; the value of R_Δ obtained from the fit; the total mass enclosed by R_Δ when it is fitted from data (note that in this case the fitted mass and the true mass refer to different radii). All these data are computed by excluding the cluster labeled C5 (see text for details).

The increase of the HE violation at large radii suggests that the mass profiles should be better recovered in normalization by limiting the fit to a smaller region, typically $\lesssim r_{500}$. This radius represents the outermost limit typically reached by X–ray observations. We repeat the analysis by limiting the fit to r_{500}, while using the recovered NFW model to extrapolate the mass profile out to the virial radius. The left panel of Figure 6 demonstrates that restricting the reconstruction of the profile within r_{500} has the expected effect of reducing the mass underestimate. While the recovered mass profiles are very close to the hydrostatic ones out to the fitting radius r_{500}, it exceeds the HE predictions at larger radii, while remaining within the 10 per cent underestimate of the true mass out to the virial radius. This demonstrates that the NFW model reconstructed within r_{500} can be safely extrapolated to larger radii to extend the mass profile reconstruction. After averaging over the set of simulated clusters, we find that M_{500} and M_{vir} are both recovered with an underestimate of only 10 per cent (see Table 2). The right panel of Figure 6 shows the accuracy in recovering the virial mass of each cluster. This plot has a larger scatter with respect to Figure 5, due to the fact the we are now fitting over mass profiles over a narrower radial range (see Table 2). In agreement with the results of Piffaretti & Valdarnini (2008), we conclude that a reliable procedure is to reconstruct the mass profiles within relatively small radii, $\sim r_{500}$, where the HE is not seriously violated, while extrapolating to so-obtained mass profile according to the NFW model.

In the results shown so far, we assumed that we exactly know the value of the radius, either r_{vir} or r_{500}, within which the masses are recovered. In the analysis of observational data, instead, the virial radius is generally not known in advance, but it is estimated directly from the recovered mass profile. Therefore, if the mass profile is under/overestimated, also the estimate of the virial radius will be biased low/high. As pointed out by Nagai et al. (2007), this turns

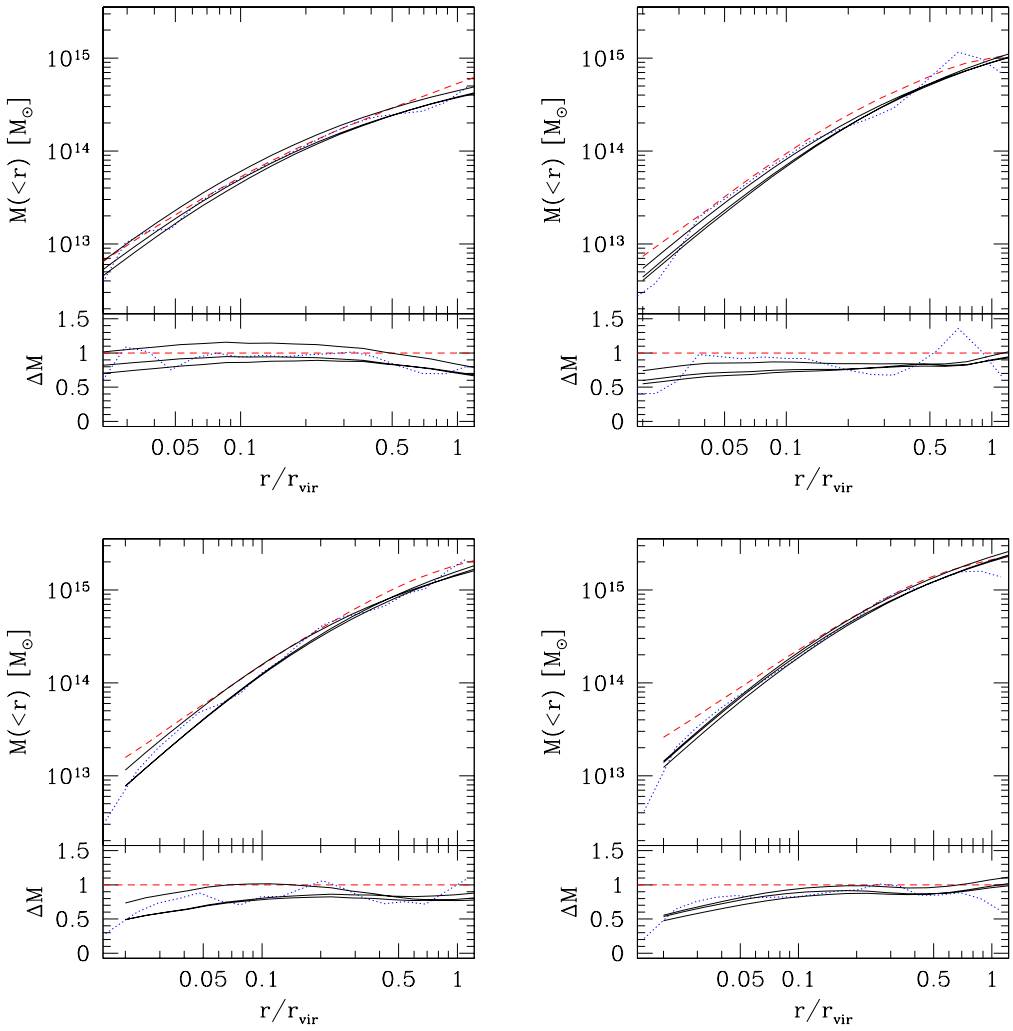

Figure 4. The reconstruction of the mass profiles for the C1, C2, C3 and C4 clusters, based on the Method 2, compared with the true profiles (dashed curves) and with the profiles recovered from the hydrostatic equilibrium (dotted curves). For each cluster, the three solid curves show the reconstruction along the three axes of projection.

out into a larger bias in the recovered M_{500} or M_{vir}. In order to quantify this effect, we show in the left panel of Figure 7 the virial radii inferred from the reconstructed mass profiles, $r_{vir,fit}$, vs. the true ones $r_{vir,sim}$. Clearly, the recovered virial radii are generally smaller than the true one, by about 10 per cent. This bias decreases by a few percent if $r_{vir,fit}$ is recovered from the extrapolation of the profile fitted within r_{500} (seeTable 2). The right panel of Figure 7 shows the recovered virial mass when using $r_{vir,fit}$ versus the true virial mass. A comparison of this plot with the right panel of Figure 5 shows that the effect of using the recovered virial radius is that of slightly increasing the underestimate of the virial mass, which is now $M_{vir,fit}/M_{vir,true} = 0.76 \pm 0.11$. Again, we verified that this effect is reduced, with $M_{vir,fit}/M_{vir,true} = 0.89 \pm 0.27$ when using instead the virial radius extrapolated from the analysis performed within r_{500}.

Finally, we find that observing the same cluster along different lines of sight cause differences in the reconstructed mass by only a few per cent (see Figures 5, 6 and 7). It is worth noting that the axes of projection are not chosen randomly, instead they are fixed to the principal axes of the inertia tensor. This choice maximizes the difference between the projected images, so our estimate can be considered an upper limit of this effect.

6 THE CONCENTRATION–MASS RELATION

In this section, we first study the c–M relation on the three–dimensional mass profiles computed directly from the simulation data, so that no observational effects are included. Then, we will show how well this relation can be reconstructed from the analysis of combined X–ray/SZ observations (using Method 2), for the subset of clusters having $T_{\rm sl} \gtrsim 3$ keV. Since the behaviour of the $c - M$ relation strongly depends on cosmological parameters, we limit our analysis to those objects belonging to the first simulation (i.e. C1, C2, C3 and from C5 to C11). Finally, we also compare our results with the mass–concentration relation proposed by Eke et al. (2001), using the cosmological parameters assumed in our simulations (see Section 2).

Figure 8 shows the c–M relation computed over the 117 clusters identified in the simulation box and having mass assigned by

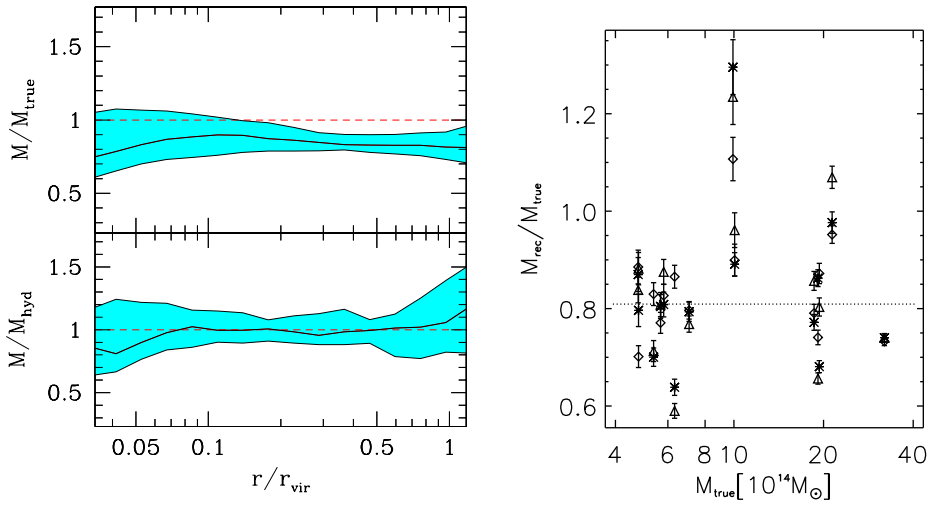

Figure 5. Left panel: the ratio of the reconstructed mass profiles, based on Method 2 (fitting out to r_{vir}), with the true (upper panel) and hydrostatic (lower panel) mass profiles, after averaging over the set of simulated clusters. The shaded area encompasses 68 per cent of the recovered profiles, while the solid line shows the median profile. Right panel: the ratio between the recovered and the true masses, both computed within r_{vir}, as a function of the true mass of each cluster. Diamonds, triangles and stars are for the reconstruction from the projection along the x, y and z axis respectively. Errorbars represent the 1σ statistical uncertainty on the recovered mass, due to the noise in mock SZ/X–ray images. The horizontal dotted line indicates the mean deviation of the reconstructed mass.

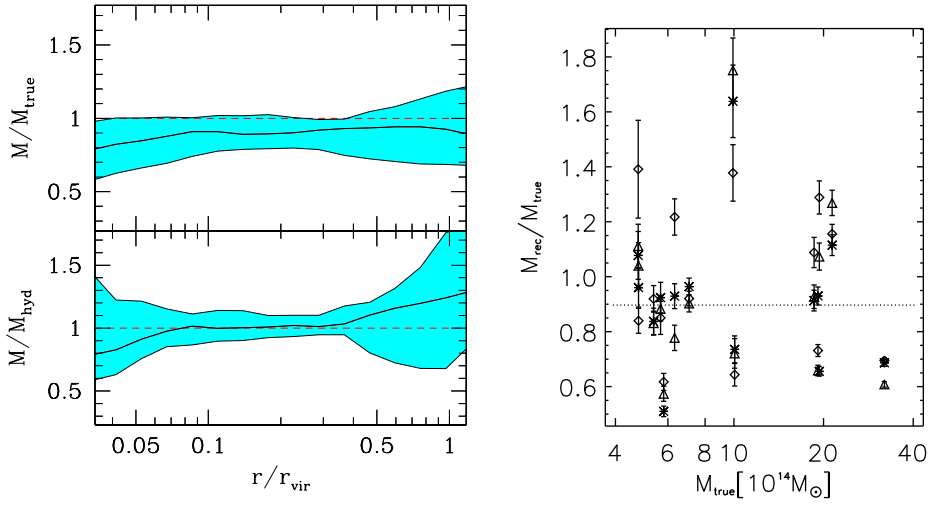

Figure 6. The same as in Figure 5, but fitting the NFW profile out to r_{500}, and extrapolating it out to r_{vir}.

a friends-of-friends algorithm above $10^{14}\,h^{-1}M_{\odot}$ (Borgani et al. 2004). The left panel of the figure shows the result of fitting the integrated mass profile to the NFW formula out to r_{vir}, while in the right panel we exclude the central region with $r < 0.05r_{vir}$. Note that excluding the inner regions from the fit has the effect of decreasing the resulting value of c, thus bringing the relation in closer agreement with that by Eke et al. (2001), which is based on purely N–body simulations. Including gas cooling and star formation leads to the formation of a stellar component, which generally has a more sharply peaked mass distribution with respect to the dark matter one. As a consequence, one observes a steepening of the total mass profile in the core, with a subsequent increase of the concentration parameter. Furthermore, gas cooling is also known to induce adiabatic contraction, i.e. a steepening of the dark matter profile in reaction to the strong increase of gas density in the core regions (e.g. Gnedin et al. 2004). We point out that the increase of c is much reduced when fitting the differential mass profiles, which gives less weight to the inner halo regions, rather than the integrated mass profile. However, the case of fitting the integrated mass is more relevant for tSZ and X–ray studies, since the application of the hydrostatic equilibrium equation gives the integrated mass profile, rather than the differential one.

In Figure 8, the colour of each symbol indicates the spectroscopic–like temperature of the corresponding cluster. We divide the clusters into 3 temperature bins. We find that hotter clusters tend to have a slightly larger c than colder ones, at a fixed mass. The effect can be seen more clearly in Figure 9, which reports the fractional deviation of the spectroscopic–like temperature, $\Delta T_{\rm sl}$,

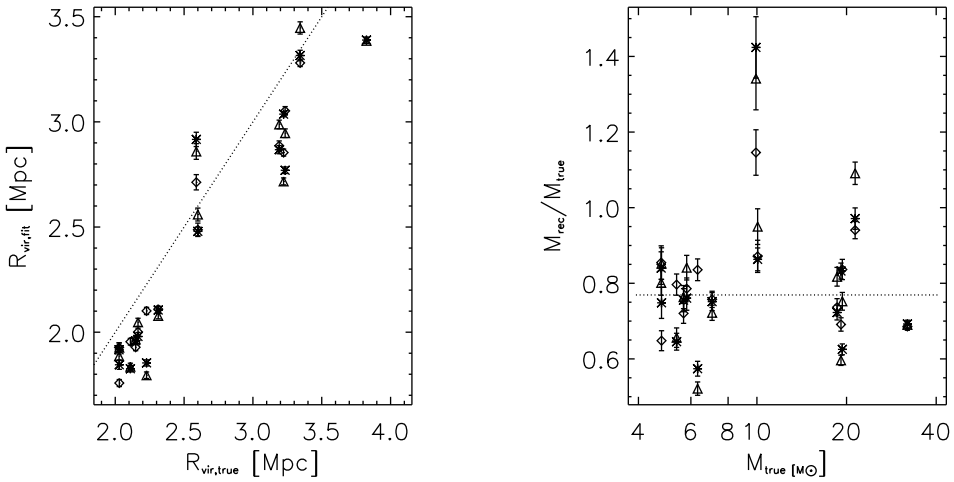

Figure 7. Left panel: the estimated virial radius $r_{vir,fit}$ using Method 2 out to r_{vir}) vs. the true one computed from the simulation data $r_{vir,sim}$. The dotted line reports the one–to–one relation. Right panel: the recovered mass within $r_{vir,fit}$ vs. the true mass within $r_{vir,sim}$. In both panels, diamonds, triangles and stars are for the reconstruction from the projection along the x, y and z axis respectively. Errorbars represent the 1σ statistical uncertainty on the recovered mass, due to the noise in mock SZ/X–ray images. The horizontal dotted line represents the mean over all the mass determinations.

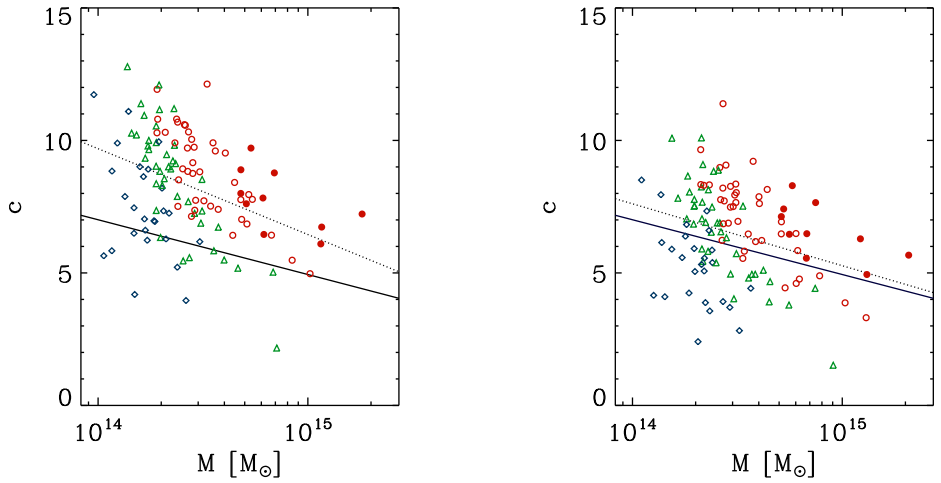

Figure 8. The concentration–mass relation for all the clusters extracted from cosmological box of Borgani et al. (2004). Diamonds, triangles and circles are for objects with $T_{\rm sl} < 1.5$ keV, $1.5 < T_{\rm sl} < 2$ keV and $T_{\rm sl} > 2$ keV, respectively. The objects used in this paper are indicated by filled symbols. In both panels the dotted line represents the least–squares fit on the points, the solid line is the model proposed by Eke et al. (2001). The left and the right panels correspond to fitting over the whole radial range, out to r_{vir}, and after excluding the central region within $0.05r_{vir}$, respectively.

and concentration Δc from the mean $T_{\rm sl}$–M and c–M relations respectively. We find that the correlation factor is quite high, with $r = 0.86$. This correlation is explained by considering that clusters with larger c have a deeper gravitational potential and thus a hotter ICM. We point out that this does not depend on the use of the spectroscopic–like temperature. In fact, when using the mass–weighted temperature, $T_{\rm mw} = \sum m_i T_i / \sum m_i$, we find that this correlation is only slightly weaker, with $r = 0.77$, but still significant. As a consequence, selecting the clusters through their (X–ray) temperature (as we do in this paper) has the effect of biasing high the recovered c–M relation.

Our results go in the opposite direction with respect to those by Yang et al. (2008), who instead find a negative correlation between temperature and concentration in a set of simulated galaxy clusters. These authors based their analysis on a cosmological box simulated with the Eulerian FLASH code. Tracing the origin of this difference between our and their results would require a detailed comparison. We note that the run analysed by Yang et al. (2008) includes quite difference physical processes: it assumes gas pre–heating at $z = 3$, while it does not include radiative cooling, star formation and stellar feedback. We also note that the size of the grid in their simulation is $250\,h^{-1}$kpc, thus implying that r_{500} in a typical cluster is sampled only with few resolution elements.

The results discussed in this paragraph and shown in Figures 10 and 11 have been obtained by applying Method 2 out to r_{vir}. The procedure is discussed in detail in Section 5.2. In Fig-

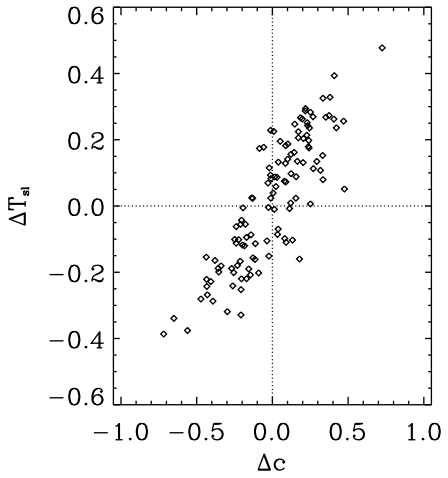

Figure 9. The correlation between the scatter in the temperature–mass relation and the scatter in the concentration–mass relation. Results are shown for the same objects as in Fig. 8.

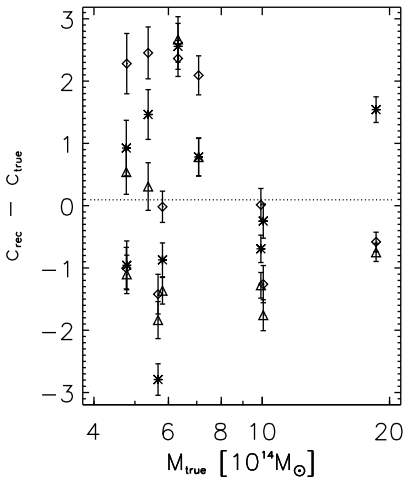

Figure 11. The difference between the recovered and the true concentration parameter as a function of the true cluster mass within r_{vir}. The errorbars show the 1σ statistical error from the recovery of the cluster mass profile.

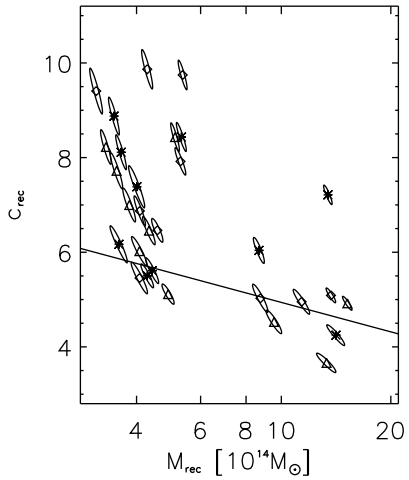

Figure 10. The concentration–mass relation recovered from deprojection. The solid line represents the model by Eke et al. (2001). The ellipses show the 1σ confidence regions. Diamonds, triangles and stars are for the reconstruction from the projection along the x, y and z axis respectively

ure 10 we show the c–M relation, as it would be recovered from the deprojection of SZ/X–ray images. We find that it is systematically higher than the expected one. This shift is due to the temperature cut in selecting clusters, which tends to favor more concentrated systems. Finally, we show in more detail in Figure 11 our results on the concentration parameter. We report the error on c as a function of the cluster mass. We find that $\langle c_{rec} - c_{true} \rangle = 0.1 \pm 1.5$, with no significant trend with the cluster mass. This result demonstrates that the value of c is recovered unbiased on average, although with a fairly large scatter.

7 CONCLUSIONS

Correctly measuring the total collapsed mass of galaxy clusters is of fundamental importance for these objects to be used as tools for precision cosmology. In cluster studies based on the observations of the intra–cluster medium (ICM) the mass is inferred by applying the equation of hydrostatic equilibrium (HE) under the assumption of spherical symmetry, thus requiring that both the gas density and the temperature profiles are measured to good accuracy. The observational analyses carried out to so far are essentially based on X–ray data. Although X–ray surface imaging provides robust measurements of the gas density profiles out to a significant fraction of the cluster virialized regions, temperature measurements from spatially resolved X–ray spectroscopy are in general much noisier and restricted to smaller radii. In this paper we addressed the issue of measuring cluster masses by using a combination of Sunyaev–Zeldovich (SZ) and X–ray imaging, thereby avoiding X–ray spectroscopy.

To this purpose we presented in this paper a development of the maximum–likelihood deprojection technique described by Ameglio et al. (2007), in which we implemented the solution of the hydrostatic equilibrium equation, so as to derive profiles of gas density, temperature and total mass simultaneously. We applied this method to cosmological hydrodynamical simulations of galaxy clusters. After quantifying the intrinsic level of HE violation in our simulations, we applied two different methods to recover the total mass profile from the deprojection of SZ and X–ray maps, both methods being based on the assumption of HE. Method 1 adopts a model–independent approach, in which the fitting parameters are represented by the values of the gas density and total mass profiles within 15 radial bins, with the only constraint of increasing mass with radius. Method 2 is instead based on assuming the mass profile by Navarro et al. (1997) (NFW). In this case, the mass profile is characterized by only 2 fitting parameters, namely the concentration c and the total mass M.

The main results of our analysis be summarized as follows.

• In keeping with previous analyses (e.g. Rasia et al. 2004; Kay et al. 2004; Rasia et al. 2006; Nagai et al. 2007; Piffaretti & Valdarnini 2008), we find that deviations from hydro-

static equilibrium are quite common in simulated clusters, due to the presence of pressure support associated to stochastic and bulk gas motions. These deviations lead to an average mass underestimate of about 10 per cent within r_{500}. It increases at larger radii, reaching about 20 per cent at r_{vir}, due to the presence of ongoing mergers and continuous gas accretion, which characterize the cluster outskirts.

- From Method 1, we find that in the inner regions (out to about $r = 0.15 r_{vir}$) the mass is recovered with an underestimate of about 10–15 per cent, largely due to the violation of hydrostatic equilibrium. On the other hand, the reconstructed mass becomes closer to the true one when moving to the outskirts. In this case, the effect of noise in the deprojection algorithm tends to compensate the underestimate due to the violation of the hydrostatic equilibrium. Generally, the fairly large number of fitting parameters causes a significant scatter (about 15 per cent) in the recovered mass profiles.
- As for the Method 2, we find that the total mass is underestimated by a larger amount, about 20 per cent, when the deprojection is performed from r_{vir}. Indeed, using a fixed NFW functional form for the mass profile forces the mass underestimate found at the outermost radius to propagate to smaller radii. Therefore, the overall lower normalization of the mass profile is just the consequence of the larger violation of the HE found at r_{vir}. On the other hand, assuming a fixed functional form for the mass profile leads to a more stable, although more biased, reconstruction, with a scatter of about 10 per cent, thus lower than found with Method 1.
- As expected, fitting the model profiles in the deprojection within r_{500} and extrapolating out to the virial radius is a safer procedure, thus in agreement with the results by Piffaretti & Valdarnini (2008). The mass underestimate is reduced to ~ 10 percent, but at the expense of increasing the cluster-to-cluster scatter to about 20 per cent.
- We verified that the choice of the line of sight generally affects the mass reconstruction. With Method 1, we show that the mass reconstructed from the projection performed along the maximum elongation axis is generally larger, by about 10 per cent, than from the other two projection directions. Using instead Method 2, we find that the typical scatter between the masses reconstructed from different projections of the same cluster is typically of only a few percent.
- The relation between concentration parameter of the NFW density profile and cluster mass shows a strong correlation with the temperature of the cluster: at a fixed mass, hotter clusters tend to be more concentrate. For this reason, in our selection of clusters having $T_{\rm sl} \geqslant 3$ keV we find a $c - M$ relation having higher normalization than that calibrated from N–body simulations (e.g., Eke et al. 2001).
- Using Method 2, the concentration parameter of the NFW profile is recovered on average without any significant bias, but with a significant scatter of $\Delta c \simeq 1.5$.

Our results lend support to the efficiency of combining X–ray and tSZ imaging data to recover the total mass profiles of galaxy clusters. In fact, the main bias that we found is intrinsic, since it is due to deviations from perfect hydrostatic equilibrium. This approach has several advantages with respect to the traditional one based on X–ray spectroscopy. Firstly, the temperature recovered from the fit of the X–ray spectra generally differs from the electron temperature, by an amount which depends on the degree of complexity of the ICM thermal structure (e.g., Mazzotta et al. 2004; Vikhlinin 2006). Secondly, X–ray surface brightness profiles can be obtained with good precision with a relatively small number of photon counts ($\sim 10^2$), while at least ten times more photons are required for a reliable spatially resolved spectroscopy. Also, once the cosmic and instrumental backgrounds are under control, this opens the possibility of tracing the surface brightness over a large portion of the cluster virial regions, as already demonstrated with ROSAT-PSPC imaging data (e.g., Vikhlinin et al. 1999; Neumann 2005). Since the tSZ has the potential of covering a large range in gas density, its combination with low–background X–ray imaging data would allow one to better characterize the outskirts of galaxy clusters. Moreover, another advantage is that the tSZ is independent of redshift, so its combination with X–ray surface brightness will substantially improve the analysis of cluster properties at high redshift, where accurate X–ray spectroscopy may be very hard, if not impossible, to obtain.

A limitation of the analysis presented in this paper is that we did not include realistic backgrounds in the generation of the X–ray and tSZ maps. As we have just mentioned, there are interesting perspectives for a good characterization of the X–ray background. However, the situation could be more complicated for the tSZ background. In this case, contaminating signals from unresolved point–like radio sources (e.g., Bartlett & Melin 2006) and fore/background galaxy groups (e.g., Hallman et al. 2007) could affect the tSZ signal in the cluster outskirts. In this respect, the possibility of performing multi–frequency observations with the good angular resolution offered by interferometric techniques will surely help in characterizing and removing these contaminations.

Single–dish sub-millimetric telescopes of the next generation promise to provide tSZ images of clusters with a spatial resolution of few tens of arcsec, while covering fairly large field of views, with 10–20 arcmin aside, with a good sensitivity. At the same time, future satellites for X–ray surveys (e.g. eROSITA) will have the capability of surveying large areas of the sky with high sensitivity and good control of the background. These observational facilities will open the possibility of carrying out in survey mode high–quality tSZ and X–ray imaging for a large number of clusters. The application of deprojection methods, like those presented in this paper will provide reliable determinations of both the gas mass and total mass profiles. This will greatly help to fully exploit the potentiality of galaxy clusters as tools for precision cosmology.

ACKNOWLEDGMENTS.

We thank Giuseppe Murante and Elena Rasia for useful discussions. The simulations have been carried out at the "Centro Interuniversitario del Nord-Est per il Calcolo Elettronico" (CINECA, Bologna), with CPU time assigned thanks to an INAF–CINECA grant and to an agreement between CINECA and the University of Trieste. This work has been partially supported by the INFN PD-51 grant, by the INAF-PRIN06 Grant and by a ASI–AAE grant. We acknowledge the financial contribution from contracts ASI-INAF I/023/05/0 and I/088/06/0.

REFERENCES

Ameglio S., Borgani S., Pierpaoli E., Dolag K., 2007, MNRAS, 382, 397
Bartlett J. G., Melin J.-B., 2006, A&A, 447, 405
Borgani S., 2006, ArXiv Astrophysics e-prints

Borgani S., Dolag K., Murante G., Cheng L.-M., Springel V., Diaferio A., Moscardini L., Tormen G., Tornatore L., Tozzi P., 2006, MNRAS, pp 270–+
Borgani S., Murante G., Springel V., Diaferio A., Dolag K., Moscardini L., Tormen G., Tornatore L., Tozzi P., 2004, MNRAS, 348, 1078
Bouchet L., 1995, A&AS, 113, 167
Bullock J., Kolatt T., Sigad Y., Somerville R., Kravtsov A., Klypin A., Primack J., Dekel A., 2001, MNRAS, 321, 559
Cavaliere A., Fusco-Femiano R., 1976, A&A, 49, 137
Croston J. H., Arnaud M., Pointecouteau E., Pratt G. W., 2006, A&A, 459, 1007
De Filippis E., Sereno M., Bautz M. W., Longo G., 2005, ApJ, 625, 108
Dolag K., Bartelmann M., Perrotta F., Baccigalupi C., Moscardini L., Meneghetti M., Tormen G., 2004, A&A, 416, 853
Dolag K., Jubelgas M., Springel V., Borgani S., Rasia E., 2004, ApJ, 606, L97
Eke V. R., Cole S., Frenk C. S., 1996, MNRAS, 282, 263
Eke V. R., Navarro J. F., Steinmetz M., 2001, ApJ, 554, 114
Ettori S., De Grandi S., Molendi S., 2002, A&A, 391, 841
Gastaldello F., Buote D. A., Humphrey P. J., Zappacosta L., Bullock J. S., Brighenti F., Mathews W. G., 2007, ApJ, 669, 158
Gilks W., Richardson S., Spiegelhalter D., 1996, Markov Chain Monte Carlo in practice. Chapman and Hall
Gnedin O. Y., Kravtsov A. V., Klypin A. A., Nagai D., 2004, ApJ, 616, 16
Haiman Z., Mohr J. J., Holder G. P., 2001, ApJ, 553, 545
Hallman E. J., O'Shea B. W., Burns J. O., Norman M. L., Harkness R., Wagner R., 2007, ArXiv e-prints, 704
Jeltema T. E., Hallman E. J., Burns J. O., Motl P. M., 2007, ArXiv e-prints, 708
Kay S. T., Thomas P. A., Jenkins A., Pearce F. R., 2004, MNRAS, 355, 1091
Lee J., Suto Y., 2004, ApJ, 601, 599
MacKay D., 1996, Markov Chain Monte Carlo in practice. Chapman and Hall
Mandelbaum R., Seljak U., Hirata C. M., 2008, Journal of Cosmology and Astro-Particle Physics, 8, 6
Mazzotta P., Rasia E., Moscardini L., Tormen G., 2004, MNRAS, 354, 10
Morandi A., Ettori S., 2007, MNRAS, 380, 1521
Morandi A., Ettori S., Moscardini L., 2007, MNRAS, pp 541–+
Mroczkowski T., Bonamente M., Carlstrom J. E., Culverhouse T. L., Greer C., et al. 2008, ArXiv e-prints
Nagai D., Vikhlinin A., Kravtsov A. V., 2007, ApJ, 655, 98
Navarro J., Frenk C., White S., 1997, ApJ, 490, 493
Neal R. M., , 1993, Probabilistic inference using Markov Chain Monte Carlo methods
Neumann D. M., 2005, A&A, 439, 465
Pierpaoli E., Borgani S., Scott D., White M., 2003, MNRAS, 342, 163
Piffaretti R., Valdarnini R., 2008, ArXiv e-prints, 808
Pointecouteau E., Arnaud M., Pratt G. W., 2005, A&A, 435, 1
Pointecouteau E., Hattori M., Neumann D., Komatsu E., Matsuo H., Kuno N., Böhringer H., 2002, A&A, 387, 56
Pratt G. W., Arnaud M., 2002, A&A, 394, 375
Puchwein E., Bartelmann M., 2007, A&A, 474, 745
Rasia E., Ettori S., Moscardini L., Mazzotta P., Borgani S., Dolag K., Tormen G., Cheng L. M., Diaferio A., 2006, MNRAS, 369, 2013
Rasia E., Tormen G., Moscardini L., 2004, MNRAS, 351, 237
Rosati P., Borgani S., Norman C., 2002, ARAA, 40, 539
Schmidt R. W., Allen S. W., 2007, MNRAS, 379, 209
Springel V., 2005, ArXiv Astrophysics e-prints
Springel V., Hernquist L., 2003, MNRAS, 339, 289
Vikhlinin A., 2006, ApJ, 640, 710
Vikhlinin A., Forman W., Jones C., 1999, ApJ, 525, 47
Vikhlinin A., Kravtsov A., Forman W., Jones C., Markevitch M., Murray S. S., Van Speybroeck L., 2006, ApJ, 640, 691
Voit G. M., 2005, Reviews of Modern Physics, 77, 207
Yang H. ., Ricker P. M., Sutter P. M., 2008, ArXiv e-prints, 808
Yoshida N., Sheth R., Diaferio A., 2001, MNRAS, 328, 669
Zappacosta L., Buote D. A., Gastaldello F., Humphrey P. J., Bullock J., Brighenti F., Mathews W., 2006, ApJ, 650, 777
Zaroubi S., Squires G., de Gasperis G., Evrard A. E., Hoffman Y., Silk J., 2001, ApJ, 561, 600
Zhang T.-J., Wu X.-P., 2000, ApJ, 545, 141